

## **Supplementary Information**

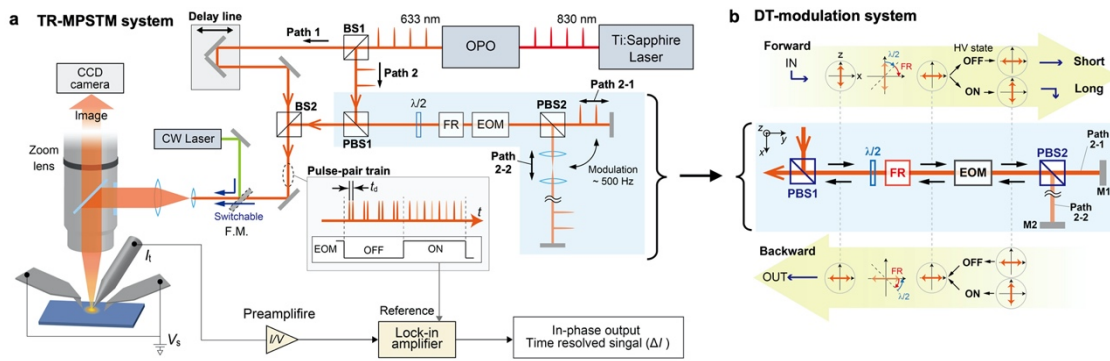
### **Ultrafast nanoscale exciton dynamics via laser-combined scanning tunneling microscopy in atomically thin materials**

Hiroyuki Mogi<sup>1</sup>, Yusuke Arashida<sup>1</sup>, Ryusei Kikuchi<sup>1</sup>, Ryosuke Mizuno<sup>1</sup>, Jun Wakabayashi<sup>1</sup>, Naoki Wada<sup>2</sup>, Yasumitsu Miyata<sup>2</sup>, Atsushi Taninaka<sup>1</sup>, Shoji Yoshida<sup>1</sup>, Osamu Takeuchi<sup>1</sup>, and Hidemi Shigekawa<sup>1</sup>

<sup>1</sup> *Faculty of pure and applied sciences, University of Tsukuba, Tsukuba, Ibaraki 305-8573, Japan*

<sup>2</sup> *Department of Physics, Tokyo Metropolitan University, Hachioji, Tokyo 192-0397, Japan*

## Supplementary Figures



**Supplementary Figure 1: Schematic of the newly developed TR-MPSTM.** **a**, TR-MPSTM system. BS (beam splitter), PBS (polarized beam splitter), OPO (optical parametric oscillator), FR (Faraday rotator), EOM (electro-optical modulation element). **b**, Principle of newly designed delay-time (DT) modulation system, which significantly increases SN ratio. M1, M2: mirror 1 and mirror 2. See Methods for details.

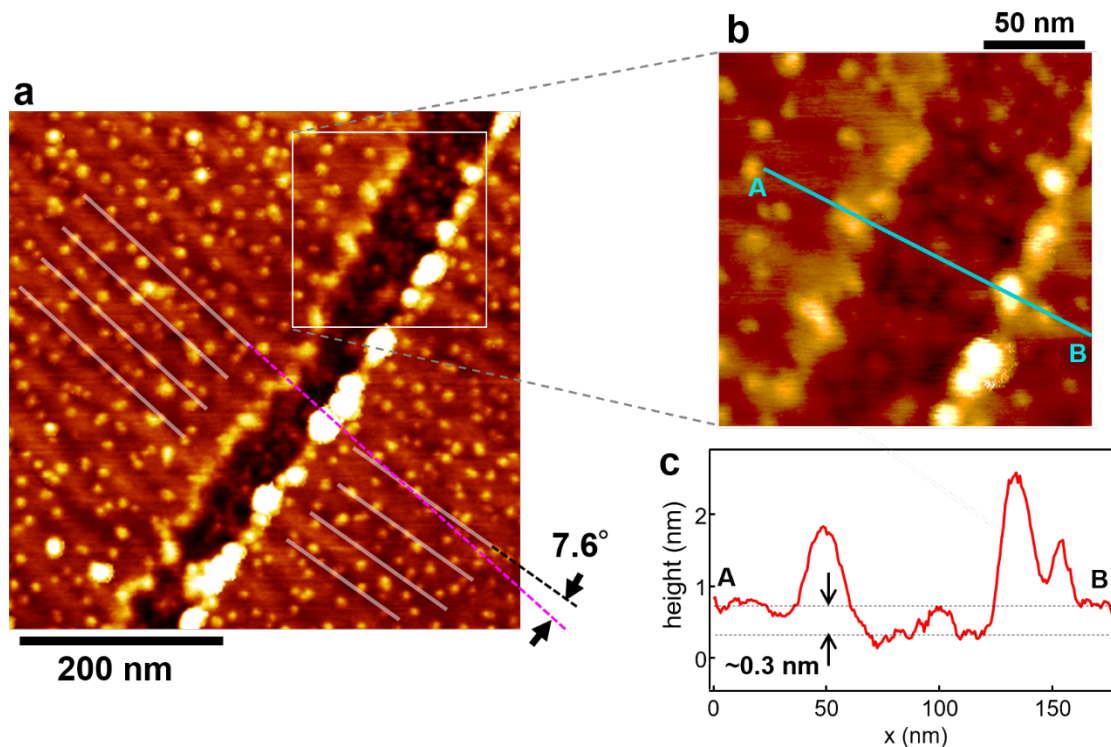
In time-resolved STM, a modulation method for lock-in detection is indispensable. We found it necessary to shorten the measurement time to stably measure the weak signal of excitons and enable two-dimensional imaging. Therefore, we developed a new delay time modulation system and increased the light intensity by 80 times and the signal-to-noise ratio.

Figure S1b shows the principle of our new delay-time modulation system (DT modulation system) that modulates the light passing through Path 2 shown in the blue shaded area in Fig. S1a. The figures in the upper and lower yellow arrows show the changes in polarized light (red arrows) in the direction from PBS1 to PBS2 (forward) and the direction from PBS2 to PBS1 (backward), respectively.

In PBS1, only linearly polarized light in the z-direction is reflected. The plane of polarization

is rotated by  $90^\circ$  by the  $\lambda/2$  wave plate and the Faraday rotator (FR) and is incident on the EOM. When no high voltage (HV) is applied to the EOM (OFF), the light beam passes through PBS2 while maintaining the plane of polarization (Path 2-1). When HV is applied to the EOM (ON), the plane of polarization of the light beam is rotated  $90^\circ$  and reflected by PBS2 (Path 2-2). In both paths, the mirrors (M1 and M2) placed perpendicular to the optical path reflect the two light beams and they merge at PBS2. As a result, the optical path length can be modulated by selecting Path 2-1 with a short optical path length and Path 2-2 with a long optical path length depending on the presence or absence of the applied voltage to the EOM. The optical path length difference between Path 2-1 and Path 2-2 is 1.8 m (a time of  $\sim 6$  ns). Since the plane of polarization rotates in the backward direction when HV applied to the EOM is ON, polarization in the x-direction is obtained after the light beam passes through the EOM regardless of whether or not HV is applied. After that, since the rotation directions of the polarization planes induced by the  $\lambda/2$  wave plate and FR are opposite, the polarization planes are not rotated, and the polarization in the x-direction is maintained. Therefore, the light beam reflected by PBS1 and traveling in the forward direction is now directed toward BS2, which is  $90^\circ$  different from that of the incident beam.

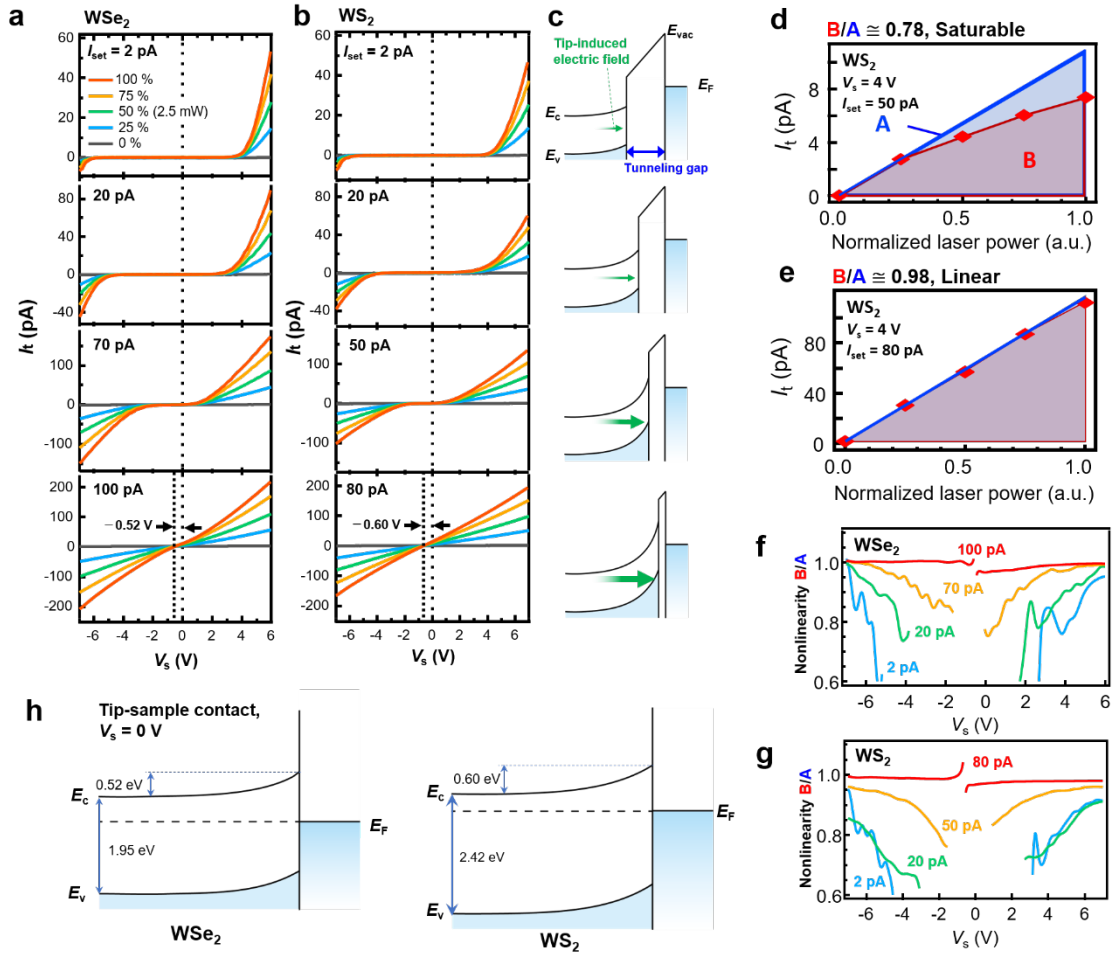
The light emitted from the delay-time modulation system merges with the light passed through Path1 at BS2 to form a pulse-pair train with delay-time modulation, as shown in Supplementary Fig. 1a. We used a DG645 digital delay/pulse generator (Stanford Research Systems, Inc.) and a JK-Flip Flop in toggle mode to adjust the ON/OFF of the EOM driver (DPD-300-4.6-A1, Eksma Optics) and control the frequency and phase of the delay time.



**Supplementary Figure 2: AFM image of the grain boundary (GB) shown in Fig. 3 a.**

A large-scale AFM image of the GB shown in Fig. 3a taken in air before cleaning the surface. Small dots are adsorbates deposited on the surface during the growth process. They do not have a triangular form and could be removed with the cleaning method<sup>1</sup> using the STM tip in the present case. **b.** A magnified AFM image of the GB, showing a complex structure similar to that reported in a previous paper<sup>2</sup>. Since the STM image depends on the electronic structure and bias voltage, the AFM image was measured.

Detailed analysis of the relationship between the GB structure and the exciton dynamics is attractive, which, however, is beyond the scope of this work. We leave this issue for future studies. See Supplementary Fig. 7 for the modulation of the ripple structure near the GB edge.



**Supplementary Figure 3: Tunnel current characteristics due to exciton dissociation. a,** Light-modulated scanning tunneling spectroscopy (LM-STs) spectra obtained for various setpoint currents  $I_{\text{set}}$  for  $\text{WSe}_2$  and  $\text{WS}_2$ , respectively. To reduce the thermal expansion<sup>3,4</sup>, current-voltage ( $I$ - $V$ ) measurement was performed while changing the light intensity as 50% (2.5 mW)  $\rightarrow$  100  $\rightarrow$  0  $\rightarrow$  75  $\rightarrow$  25 every 1 ms<sup>5</sup>. **c,** Schematic illustration of the band structures for various STM tip-sample distances determined by  $I_{\text{set}}$ . **d, e,** Relationship between light intensity and tunnel current. Using the  $IV$  curves shown in a and b, the current values for five light intensities at each voltage were obtained for each set current  $I_{\text{set}}$ . A denotes the value obtained by integrating the straight blue line in the figure, which was extrapolated from the current values for the light

intensities of 0% and 25% and B denotes the integrated value using the actual plot. **f, g**, B/A obtained for WSe<sub>2</sub> and WS<sub>2</sub>, respectively, for different  $V_s$  and  $I_{set}$ . **h**, Schottky barriers obtained for WSe<sub>2</sub> and WS<sub>2</sub>.

We investigated the mechanism of exciton dissociation with a high binding energy by the electric field generated by the bias voltage applied between the STM tip and the sample. The tunnel current should depend on the strength of the electric field that induces exciton dissociation and the number of excitons, determined by the light intensity. Therefore, the dependences of the tunnel current on the bias voltage and light intensity were investigated. The linearity of the signal intensity with the light intensity is also very important information in performing the optical pump-probe method.

In each region of WS<sub>2</sub> and WSe<sub>2</sub>, LM-STs measurement<sup>5</sup> was performed under the feedback conditions of  $V_s = -7$  V, light source wavelength of 532 nm, and an energy intensity of 2.5 mW. Figures S3a and S3b show typical results of LM-STs measured at locations in WSe<sub>2</sub> and WS<sub>2</sub> with different set currents ( $I_{set}$ ) and results averaged over 256 measurements, respectively. In the WS<sub>2</sub> region, measurements were taken near the top of the ripples. Compared with the STM setup, which measures conductive samples, the applied voltage here is very large ( $V_s = -7$  V), which is the field emission region in a general STM setup<sup>6</sup>. However, in this measurement, the bias voltage is divided into the tunnel junction, the inside of the sample, and the electrode-sample interface resistance. Therefore, the STM measurement is performed in the tunnel region rather than in the field emission region.

If the set current  $I_{set}$  was low, a large gap was visible in the  $I$ - $V$  curve. Therefore, it is considered that there is no influence of the free carriers generated by the light irradiation. However, from the results of the LM-STs shown in Figs. S3a and S3b, the gap voltage region of both WSe<sub>2</sub> and WS<sub>2</sub> becomes narrower as the set current increases and finally becomes gapless. That is, the

$I$ - $V$  characteristics measured by conventional STM reflect the intrinsic local density of states of the material, but in this case, the gap voltage is strongly dependent on the probe-sample distance, which depends on  $I_{\text{set}}$ . To clarify the reason for this, in this experiment, we consider the in-plane tip induced band bending (TIBB) introduced by the voltage applied between the STM tip and the sample and the mechanism of carrier generation caused by charge separation in the area.

First, it is known that when a TMDC is irradiated with light, excitons with a very large binding energy ( $\sim 0.3$  eV for  $\text{WS}_2$  and  $\text{WSe}_2$  on  $\text{SiO}_2$ ) are generated<sup>7</sup>, and an electric field above a certain level is required to cause charge separation. Therefore, when the distance between the STM tip and the sample is large and the electric field in the sample is weak, a nonlinearity appears, where the current suddenly increases when  $V_s$  exceeds a certain value (threshold value). With the approach of STM tip, as shown in Supplementary Figs. 3a and 3b, exciton dissociation occurs at lower  $V_s$ , and a smaller gap voltage is observed. As shown in Supplementary Fig. 3c, this corresponds well with the decrease in the tunnel resistance and the increase in the electric field introduced into the sample plane as the STM tip approaches the sample.

Furthermore, to confirm the relationship between the light intensity and the tunnel current, the linearity of the current response with the light intensity was analyzed. Using the  $I$ - $V$  curves shown in Supplementary Figs. 3a and 3b, the current values for five light intensities at each voltage were obtained for each set current  $I_{\text{set}}$ . Supplementary Figs. 3d and 3e show the results obtained for  $\text{WS}_2$  for  $V_s = 4$  V when  $I_{\text{set}} = 50$  and 80 pA, respectively. In the figures, A denotes the value obtained by integrating the straight blue line in the figure, which was extrapolated from the current values for the light intensities of 0% and 25% and B denotes the integrated value using the actual plot. The values of B/A are 0.78 and 0.98 for Supplementary Figs. 3d and 3e, respectively. B/A is considerably smaller than 1 when the saturation tendency is strong (Supplementary Fig. 3d) and near 1 when it is linear (Supplementary Fig. 3e). Supplementary

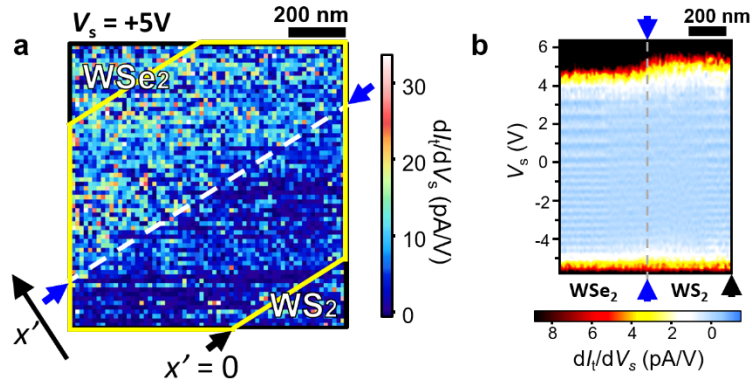
Figs. 3f and 3g show the values of  $B/A$  obtained for different values of  $V_s$  and  $I_{set}$ . The measurement points in the gap voltage region where almost no current flows were observed were omitted because of the large error. When the distance between the STM tip and the sample was large, namely  $I_{set}$  was small or  $V_s$  was low, the saturation tendency was observed ( $B/A < 1$ ). On the other hand, as the distance between the STM tip and the sample decreased, namely  $I_{set}$  was large or  $V_s$  increased,  $B/A$  tended to approach 1 and a linear response was shown.

Under an ideal constant electric field, the photocurrent generated by charge separation will be proportional to the number of incident photons ( $B/A = 1$ ). Since the effective permittivity increases as the number of excitons inside the single-layer sample increases owing to light irradiation, the increase in the internal electric field is suppressed by screening. Therefore, when the electric field generated in the sample is weak, it is insufficient to dissociate excitons, and it is considered that  $B/A$  becomes saturated. It was found  $B/A$  tends to be more saturated for  $WS_2$  than for  $WSe_2$ . In the ripple structure in the  $WS_2$  region, the distance from the substrate to the  $WS_2$  film increases periodically, and the state of the film at a long distance from the substrate is close to free standing. On the other hand, it has been reported that the absorbance tends to be higher in the free-standing state than for the case of a fused silica substrate<sup>8</sup>. Therefore, this difference in  $B/A$  is considered to be due to the higher exciton density in  $WS_2$ , which is located farther from the substrate. That corresponds well with that exciton dissociation is difficult in  $WS_2$  than in  $WSe_2$ . According to these considerations, the measured current can be explained by the dissociation of excitons induced under the STM tip.

When the STM tip and the sample were closest to each other, the voltage at which the current became zero was -0.52 V for  $WSe_2$  and -0.60 V for  $WS_2$ , as shown in Supplementary Figs. 3a and 3b. This is thought to correspond to the open-circuit voltage generated by the built-in electric field, where a Schottky barrier was created between the STM tip and the sample. Supplementary Fig.

3h shows the band structure based on these values. For the bandgap values, those from the previous paper were used<sup>9</sup>. For bulk samples, Schottky barriers are required for normal  $I$ - $V$  measurements<sup>10</sup>, but it has been shown that evaluation is possible in this way, even for single-layer samples that do not have sufficient free carriers.

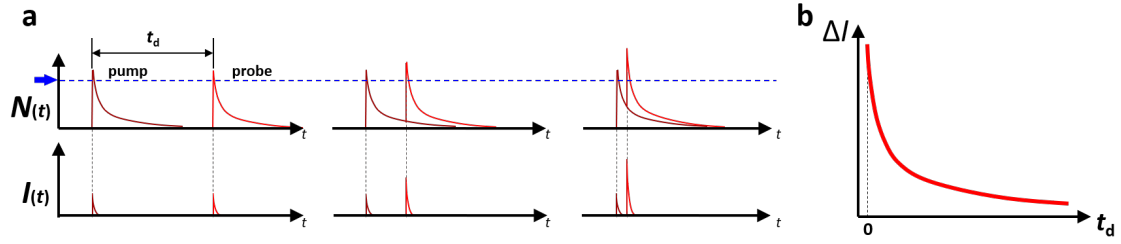
In the previous paper<sup>11</sup>, since the probe was brought into contact with the sample with a higher voltage, a strong electric field was applied over the wide depletion layer region, as shown in Fig. 4 of ref. 11. Therefore, in ref. 11, excitons generated in that region were immediately dissociated, and phenomena such as pair annihilation of excitons were not observed.



**Supplementary Figure 4: Two dimensional  $dI/dV$  mapping results.** **a**,  $dI/dV$  mapping extracted for the area shown in Fig. 2c under the condition of  $V_s = +5$  V. **b**, One-dimensional  $dI/dV$  map obtained from **a**. A straight line parallel to the interface was considered at intervals of 21 nm from the  $WS_2/WSe_2$  interface in **a**, and  $dI/dV$  was averaged over the region of  $\pm 15$  nm width from each straight line. This map summarizes the results obtained by repeating the same operation over the area surrounded by the yellow lines in **a**.

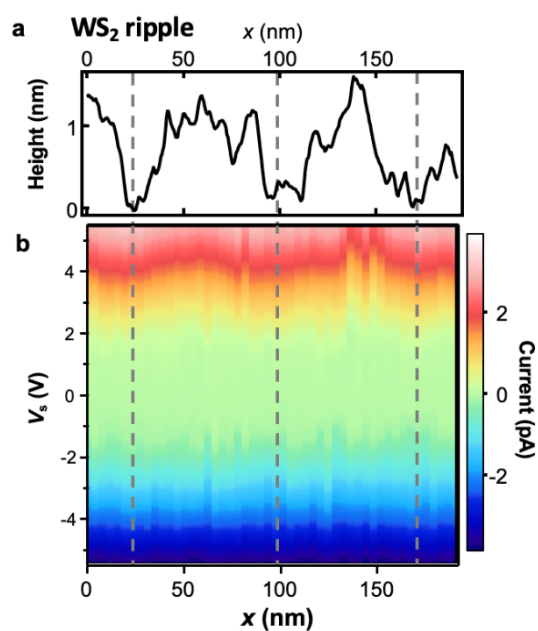
The spatial mapping of the  $I$ - $V$  curve was acquired on a grid in the same area as the STM observation shown in Fig. 2c. Supplementary Fig. 3a shows the  $dI/dV$  map extracted under the condition  $V_s = +5$  V to visualize the gap voltage width. The white dashed line shows the line of the heterojunction interface. There is a clear difference in the  $dI/dV$  values between  $WSe_2$  and  $WS_2$  regions, but  $dI/dV$  is relatively uniform within each region. Supplementary Fig. 3b shows a one-dimensional  $dI/dV$  map obtained by integrating and averaging the  $dI/dV$  curves in the direction parallel to the straight line of the heterojunction interface (dashed line in the figure). The gap voltage region is clear, and the gap in the  $WS_2$  region is larger than that in the  $WSe_2$  region. This is consistent with the exciton dissociation being more difficult in  $WS_2$  than in  $WSe_2$ , as shown in Figs. 3d to 3f. In the ripple structure in the  $WS_2$  region, the screening effect from the substrate was weakened and the binding energy increased. As shown in Supplementary Fig. 3b,

the WSe<sub>2</sub>/WS<sub>2</sub> interface is steep and is in good agreement with the STM image in Fig. 2c and the results of previous research papers<sup>12</sup>. These data were derived from the *I-V* curves and define the voltages at which excitons dissociate. Therefore, in an equilibrium state, the desired values can be obtained.

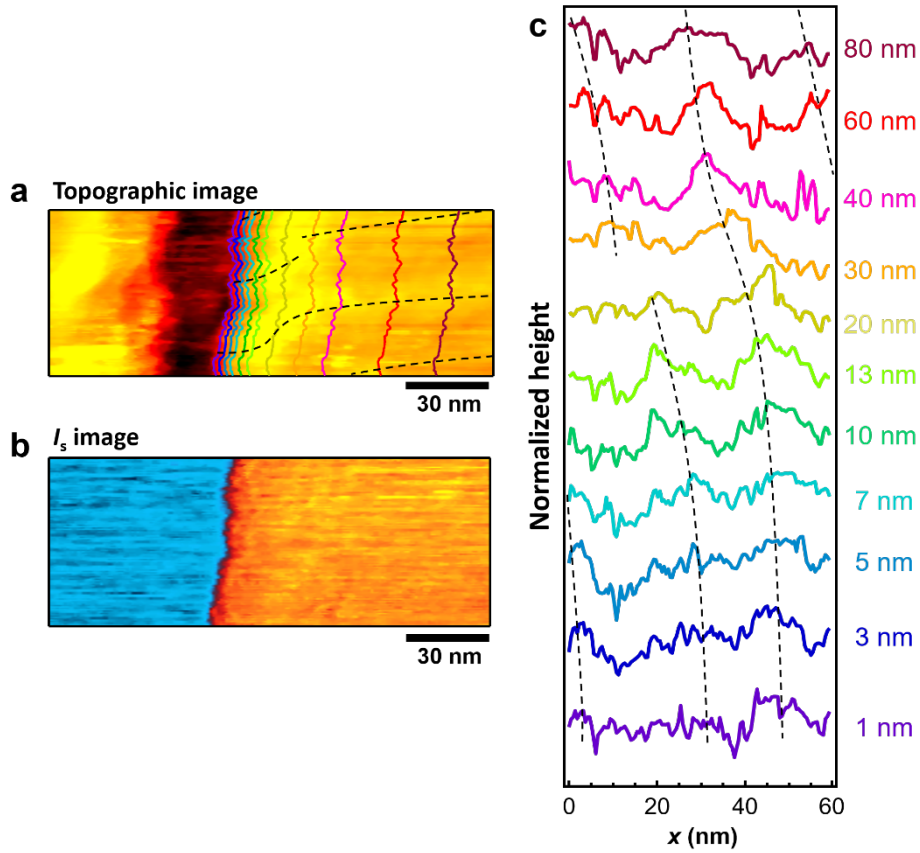


**Supplementary Figure 5: Schematic model to explain the TR-MP-STM signal.** **a**, Delay time dependence of the dynamics of exciton density  $N(t, t_d)$  excited by a pulse pair of pump and probe light.  $N(t, t_d)$  shapes for three different values of  $t_d$  are shown as examples.  $N(t, t_d)$  above the threshold blue line is detected as tunnel current  $I(t, t_d)$ . **b**, TR-MP-STM signal  $\Delta I(t_d)$  based on the mechanism shown in a, where  $\Delta I(t_d)$  is the integral of  $I(t, t_d)$  for  $t$  over the detection time. Delay-time modulation technique shown in Fig. S1b is used for measurement. Under the following two conditions,  $\Delta I(t_d)$  decreases with  $t_d$  unlike the case of absorption bleaching<sup>4</sup>: (1) The effect of absorption bleaching is not so large. (2) The probability of dissociation depends on the density of excitons and has a threshold.

In the previous paper<sup>11</sup>, laser excitation was carried out with a wavelength of 800 nm, close to the absorption edge of WSe<sub>2</sub>. Namely, the change in carrier density at the conduction band edge was probed, and the effect of absorption bleaching was large. On the other hand, in the present case, the excitation was carried out with a wavelength of 633 nm, and the excitons generated to a higher energy region in WSe<sub>2</sub> were supposed to relax to the conduction band edge in the fs to several tens of fs range. In addition, the average laser intensity was set to about 1/100 compared to that used in ref. 11. Therefore, the influence of absorption bleaching is considered to be small in this case.



**Supplementary Figure 6: Two-dimensional  $I$ - $V$  map obtained over a ripple area. **a**, Cross section of a ripple structure. **b**, Two-dimensional map of  $I$ - $V$  curves measured at each point along the cross section.  $I$ - $V$  curve rises at lower  $V_s$  in the area where the ripple contacts with the substrate, indicating that dissociation of excitons is easier there due to the effect of the substrate.**



**Supplementary Figure 7: Analysis of the ripple structures near the GB.** **a, b,** STM topographic and currents  $I_s$  images shown in Fig. 3a. **c,** Normalized cross-sections of the topographic image along the eleven lines in **a**, namely, at eleven different distances from the edge. The edge shape was obtained from the  $I_s$  image, which corresponds to the line along  $I_s = 2.8$  pA (almost corresponding to the flexion point of each scan line around the edge). As shown in **c**, the ripple structure is modulated near the GB edge, corresponding well with the change in the lifetime shown in Fig. 6. As can be seen in Fig. 3a,  $I_d$  was measured when the probe was in the area to the right of the right GB edge. Therefore, to reduce the influence of the structures in GB, this measurement was performed on the right side of the GB edge.

### Supplementary References

1. Chen, S. *et al.* Tip-Based Cleaning and Smoothing Improves Performance in Monolayer MoS<sub>2</sub> Devices. *ACS Omega* **6**, 4013–4021 (2021).
2. Liu, X., Balla, I., Bergeron, H. & Hersam, M. C. Point Defects and Grain Boundaries in Rotationally Commensurate MoS<sub>2</sub> on Epitaxial Graphene. *J. Phys. Chem. C* **120**, 20798–20805 (2016).
3. Takeuchi, O. *et al.* Probing subpicosecond dynamics using pulsed laser combined scanning tunneling microscopy. *Appl. Phys. Lett.* **85**, 3268 (2004).
4. Yoshida, S. *et al.* Optical pump-probe scanning tunneling microscopy for probing ultrafast dynamics on the nanoscale. *Eur. Phys. J. Spec. Top.* **222**, 1161–1175 (2013).
5. Takeuchi, O. *et al.* Microscopic description of the current–voltage characteristics of a bulk-heterojunction organic solar cell under illumination. *Appl. Phys. Express* **7**, 021602 (2014).
6. FOWLER, R. H. & NORDHEIM, L. Electron emission in intense electric fields. *Proc. R. Soc. London. Ser. A* **119**, 173–181 (1928).
7. Robert, C. *et al.* Exciton radiative lifetime in transition metal dichalcogenide monolayers. *Phys. Rev. B* **93**, 205423 (2016).
8. Li, Y. *et al.* Measurement of the optical dielectric function of monolayer transition-metal dichalcogenides: MoS<sub>2</sub>, MoSe<sub>2</sub>, WS<sub>2</sub>, and WSe<sub>2</sub>. *Phys. Rev. B* **90**, 205422 (2014).
9. Herbig, C. *et al.* Local Electronic Properties of Coherent Single-Layer WS<sub>2</sub>/WSe<sub>2</sub> Lateral Heterostructures. *Nano Lett.* **21**, 2363–2369 (2021).
10. Sotthewes, K. *et al.* Universal Fermi-Level Pinning in Transition-Metal Dichalcogenides. *J. Phys. Chem. C* **123**, 5411–5420 (2019).
11. Mogi, H. *et al.* Development of laser-combined scanning multiprobe spectroscopy and

application to analysis of WSe<sub>2</sub>/MoSe<sub>2</sub> in-plane heterostructure. *Appl. Phys. Express* **12**, 045002 (2019).

12. Duan, X. *et al.* Lateral epitaxial growth of two-dimensional layered semiconductor heterojunctions. *Nat. Nanotechnol.* **9**, 1024–1030 (2014).